Nanoscale

A quantitative model for a nanoscale switch accurately predicts thermal actuation behavior

Journal:	*Nanoscale*
Manuscript ID	NR-ART-05-2021-002873
Article Type:	Paper
Date Submitted by the Author:	05-May-2021
Complete List of Authors:	Crocker, Kyle; The Ohio State University, Department of Physics Johnson, Joshua; The Ohio State University, Interdisciplinary Biophysics Graduate Program; Imperial College London, Department of Chemistry Pfeifer, Wolfgang; The Ohio State University, Department of Physics, Department of Mechanical and Aerospace Engineering Castro, Carlos; The Ohio State University, Department of Mechanical and Aerospace Engineering, Interdisciplinary Biophysics Graduate Program Bundschuh, Ralf ; The Ohio State University, Physics, Department of Chemistry and Biochemistry, Division of Hematology of the Department of Internal Medicine, Interdisciplinary Biophysics Graduate Program, Center for RNA Biology

Journal Name

ARTICLE TYPE

Cite this: DOI: 00.0000/xxxxxxxxxx

A quantitative model for a nanoscale switch accurately predicts thermal actuation behavior †

Kyle Crocker,[a] Joshua Johnson,[bc] Wolfgang Pfeifer,[ad] Carlos Castro,[bd] and Ralf Bundschuh*[abefg]

Received Date
Accepted Date

DOI: 00.0000/xxxxxxxxxx

Manipulation of temperature can be used to actuate DNA origami nano-hinges containing gold nanoparticles. We develop a physical model of this system that uses partition function analysis of the interaction between the nano-hinge and nanoparticle to predict the probability that the nano-hinge is open at a given temperature. The model agrees well with experimental data and predicts experimental conditions that allow the actuation temperature of the nano-hinge to be tuned over a range of temperatures from 30 °C to 45 °C. Additionally, the model identifies microscopic interactions that are important to the macroscopic behavior of the system, revealing surprising features of the system. This combination of physical insight and predictive potential is likely to inform future designs that integrate nanoparticles into dynamic DNA origami structures or use strand binding interactions to control dynamic DNA origami behavior. Furthermore, our modeling approach could be expanded to consider the incorporation, stability, and actuation of other types of functional elements or actuation mechanisms integrated into nucleic acid devices.

1 Introduction

In 2006, Paul Rothemund published seminal work on the design of nanostructures out of DNA, developing a technique known as DNA origami[1]. Although early structures were static, expanding this technique to produce functional, dynamic structures has been of particular interest, since the use of DNA as a construction material renders the resulting structures naturally well-suited for use as machines in biological or synthetic systems. To this end, significant research has focused on the development of dynamic nanoscale devices[2,3]. Indeed, dynamic DNA origami devices are being developed for use as drug delivery systems[4–6], as well as molecular biological probes[7,8], computing elements, and nanorobots[2,9–11]. Interest in these applications has driven the development of a variety of actuation methods. Actuation can be achieved in a number of ways, such as introduction of short oligonucleotides with specifically designed sequences[12–14], or changing environmental factors such as salt conditions[9,15,16], pH[17–20], or temperature[9,21,22].

In order to be suitable for use in such applications, however, it is necessary to have precise control over the stimulus response, which remains challenging. To this end, we quantitatively characterize the thermal actuation of a DNA origami hinge containing a gold nanoparticle (AuNP), which was previously described by Johnson *et al.*[23]. This device consists of two stiff arms connected by a flexible vertex, such that the motion around the vertex is restricted primarily to a single angular dimension. A DNA-coated AuNP is attached to the top arm, and complementary DNA strands are affixed to the bottom arm that anneal to the AuNP to hold the hinge closed. When the temperature is increased, the hybridization between the AuNP and bottom arm melts to release the hinge into the open state. The AuNP remains stably attached to the top arm, allowing for repeatable temperature-controlled opening and closing. This type of system is of interest since AuNP-DNA origami composites have many exciting applications, such as in plasmonics[24] and nanoelectronics[25]. In particular, the potential for AuNP facilitated reconfiguration that is both fast and tunable could be important in these applications. Another area of interest for these composite devices is that they have the potential to allow for pre-

* Corresponding author.
[a] Department of Physics, The Ohio State University, Columbus, OH 43210, USA. E-mail: bundschuh@mps.ohio-state.edu
[b] Interdisciplinary Biophysics Graduate Program, The Ohio State University, Columbus, OH 43210, USA.
[c] Department of Chemistry, Imperial College London, Molecular Sciences Research Hub, 80 Wood Lane, London W12 0BZ, UK.
[d] Department of Mechanical and Aerospace Engineering, The Ohio State University, Columbus, OH 43210, USA.
[e] Department of Chemistry and Biochemistry, The Ohio State University, Columbus, OH 43210, USA.
[f] Division of Hematology, Department of Internal Medicine, The Ohio State University, Columbus, OH 43210, USA.
[g] Center for RNA Biology, The Ohio State University, Columbus, OH 43210, USA.
† Electronic Supplementary Information (ESI) available. See DOI: 00.0000/00000000.

cisely controlled local heating and therefore actuation: although the experiments described here are performed with bulk temperature change, the AuNP itself could in principle be locally heated with a laser[26]. Thus the study of systems into which such AuNPs are incorporated is a potentially fruitful area of research.

In order to design increasingly complex and useful DNA devices, it is necessary to construct predictive models of their function. This has proven to be challenging, however, since environmental factors and thermal fluctuations can play an important role, often rendering classical solid mechanics approaches common to macroscopic engineering unsuitable[2]. Nevertheless, a number of computational techniques have shown predictive efficacy. All-atom molecular dynamics (MD) simulations, which track interactions of each atom in a system over time, provide detailed and accurate information about system dynamics[27–29]. The computational cost is quite high, however, rendering such an approach practical only for small subsections of DNA devices and short time scales[2]. In order to study larger systems, one must use a coarse-grained approach. One way to do this is to approximate the atoms that make up one or more nucleotides as a single particle and track the positions and interactions of many such particles. This approach is taken most notably in the commonly used oxDNA simulations[30–33], as well as the recently developed `mrdna` model[34]. These approaches significantly extend simulation time-scales, but they are still typically limited to microsecond or at most millisecond timescales, while actuated conformational changes often occur on the second timescale or longer. Another coarse-grained approach is to use finite element (FE) modeling to predict DNA structures. A widely used example of this is CANDO[35], although this is typically used for shape prediction since it lacks molecular details that govern dynamics. Pan *et al.*[36], and more recently Lee *et al.*[37], improved on FE models with multi-scale approaches using molecular dynamics to inform local properties of structural motifs like nicks and cross-overs; these approaches provide molecular level structural insights with improved computational efficiency, but they still do not capture larger-scale conformal dynamics of reconfigurable DNA origami devices.

Long timescales or large structures may render even such coarse-grained approaches computationally unfeasible, particularly if one wants to rapidly iterate through many structural variations to guide design. It is therefore desirable to develop even more computationally efficient techniques. Here, we focus on the application of one such technique, statistical mechanics. While similar approaches have been used to model DNA strand displacement[38,39], which is widely used for actuation, application to actuation of devices themselves remain rare despite the increasing need for computational efficiency to guide design of functional DNA origami devices. In one of the few examples of application to an actual device that we are aware of, Marras *et al.* use a statistical mechanics approach to model a system in which changes in salt concentration are used to actuate a hinge[15]. Here, we develop a thermodynamic model that accurately describes the thermal actuation of the nano-hinge device containing an AuNP. To our knowledge, this is the first statistical mechanics model of a *composite* DNA origami system, which is a critical step, since many applications require the incorporation of NPs or other functional elements. Furthermore, we demonstrate that this model is able to predict actuation temperatures as a function of device design, enabling principled design of devices with desired transition temperatures. Additionally, our model gives insight into the system, demonstrating that configurational entropy and suboptimal energetic states meaningfully impact system behavior.

2 Experimental and computational methods

2.1 Experimental methods

In this subsection we describe briefly the experiments by Johnson *et al.* that provide the basis for our model[23]. The AuNP-hinge system is shown schematically in Fig. 1(A), with arrows indicating that the hinge is opened as temperature is increased and closed when temperature is decreased. In Fig. 1(B), averaged data for different overhang strand lengths are shown for hinges with two overhang strands (left), which we call “bivalent" or three overhang strands (right), which we call "trivalent". The overhang lengths (6-8 bases) and sequences (all adenine bases) are identical in the bivalent and trivalent cases.

2.1.1 Design and fabrication of DNA origami hinges

The studied DNA origami hinges and AuNP-hinge constructs were prepared as previously described[23]. Briefly, 20 nM scaffold DNA (p8064) and 200 nM staple strands were pooled in TE-buffer (5 mM Tris, 1 mM EDTA, pH 8.0, 5 mM NaCl) supplemented with 18 mM $MgCl_2$ and subjected to a thermal annealing consisting of 15 min at 65 °C following by 4 hours at 53 °C and cooling to 4 °C. Excess staple strands were removed by centrifugal purification in the presence of PEG and resuspended in TE-buffer supplemented with 12.5 mM $MgCl_2$[40]. Conjugation of T_{23} ssDNA coated AuNP, prepared as described by Johnson *et al.*[23], to the purified DNA hinges was performed by addition of 5-fold excess AuNPs to the resuspended DNA hinges and incubation at 45 °C for 15 minutes.

2.1.2 Thermal actuation

Thermal profiles of the different constructs were collected on a Cary Eclipse Fluorometer with thermostated multicell cuvette holder. If not stated otherwise, temperature ramps were set to 2 °C/min and thermal profiles were collected by cycling between the respective minimum and maximum temperatures at least twice. A reference hinge without AuNP was used to substract temperature dependent effects of the fluorophore.

2.1.3 EM Imaging

Negative stain electron microscopy was used to confirm folding and correct incorporation of AuNPs into the DNA hinges, following previously described protocols[23]. Purified DNA hinges and AuNP-hinge constructs were adsorbed onto TEM grids (Electron Microscopy Sciences, Hatfield, PA), stained using freshly prepared Uranyl-formate and imaged on a FEI Tecnai G2 Spirit TEM, operated at 80 kV.

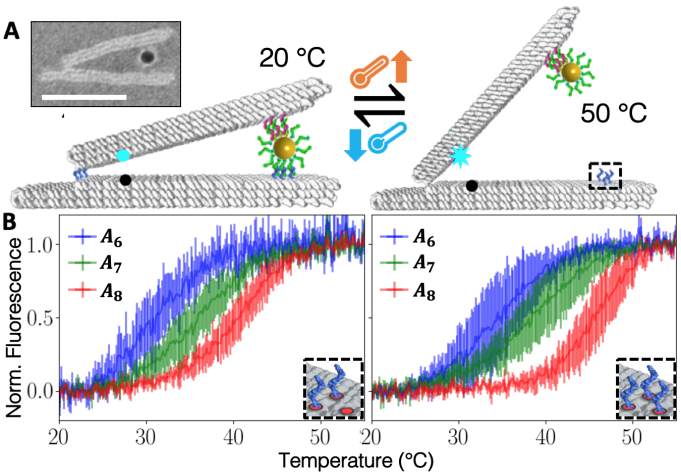

Fig. 1 Experimental system and thermal actuation data underlying our model. (A) shows the experimental system: a gold nanoparticle (AuNP) is affixed to the top arm of a DNA origami nano-hinge via long, stable dsDNA strands formed between single stranded DNA (ssDNA) overhangs on the arm and complementary strands of ssDNA coating the AuNP. Shorter overhangs on the bottom arm anneal at low temperatures and melt at high temperatures. The inset shows a TEM image of a closed hinge with AuNP at room temperature. Scale bar is 50 nm. When the bottom overhang is annealed, the hinge is forced into a closed state where fluorescence is quenched. The normalized fluorescence in (B) therefore provides a measure of the bulk fraction of hinges that are open. The insets in (B) illustrate the number of overhangs on the bottom arm of the hinge: either two ("bivalent") or three ("trivalent"). The legend indicates the sequence of the bottom arm ssDNA, for instance A_6 corresponds to a sequence consisting of 6 adenine bases. All hinge overhangs are made of adenine bases, and all AuNP connections are made of thymine bases. The lengths of bottom arm overhangs vary between 6 and 8 in both the bivalent and trivalent cases.

2.2 Data processing

2.2.1 Normalization of fluorescence

Following data collection and the subtraction of fluorescence temperature dependence, the fluorescence is normalized such that the average maximum value (corresponding to all open hinges) is equal to one and the average minimum value (corresponding to all closed hinges) is equal to zero[23].

2.2.2 Averaging of Melting and Annealing Replicates

The normalized data is averaged over all experimental replicates for both melting and annealing curves, and this average and the corresponding standard deviation are shown. Data from slightly different temperatures had to be combined due to fluctuations during thermal ramps which were set to collect one data point every 0.1 °C. Specifically, we use the temperature values of the first melting replicate and then identify the closest observed temperature values in other replicates to take the average and standard deviation of the corresponding fluorescence values. That average and standard deviation are assigned to the temperature value of the first melting replicate. In order to estimate the error due to the temperatures not lining up exactly among the replicates, we identified the maximum discrepancy in temperature values among replicates where fluorescence values are averaged, and compared the expected change in fluorescence according to our model to the experimental noise. We found that this worst case estimate of systematic error induced by averaging data from slightly different temperature values is on the order of the noise in the experimental measurements. Therefore, we concluded that any interpolation over temperature values from different replicates is unnecessary, as it would effectively constitute interpolation over noise.

2.3 Model calculation

In this section, we describe how the experimental system is modeled, both at a conceptual and mathematical level.

2.3.1 Conceptual framework

To relate the experimental readout to a calculable property of the system, we note that the fluorescence of nano-hinges, when normalized between 0 and 1, is proportional to the fraction of open nano-hinges. Furthermore, for a system in thermodynamic equilibrium, the fraction of open hinges gives the probability that an *individual* hinge is open. We therefore assume the system is in thermodynamic equilibrium and create a thermodynamic model of an individual hinge.

2.3.2 Applicability of a thermodynamic model

Before we begin to build the model, we verify that a thermodynamic model is appropriate for this system. In particular, a thermodynamic approach is only valid if there are a large number of particles in the system. At the nano-hinge level, we can estimate the number of water molecules as follows. The approximate volume of the nano-hinge is given by $V_h \approx 50\text{ nm} \times 50\text{ nm} \times 10\text{ nm} = 25{,}000\text{ nm}^3$. For water with density of about 1000 kg/m^3 and molar mass about 20 g/mol, this volume contains roughly 1 million water molecules. Furthermore, in the bulk fluorescence measurements, we measure nano-hinges at 20 nM in 50 μL of solution. The bulk measurements therefore take into account more than 100 billion nano-hinges. Since these numbers are quite large (i.e. much greater than 1), we conclude that a thermodynamic model is appropriate. Additionally, since the water bath ensures a constant temperature, the Boltzmann distribution is the appropriate distribution to describe the system.

2.3.3 Model states and parameters

As discussed in more detail in section 3.1, a thermodynamic model requires enumeration of allowed states and corresponding free energies. The experimentally observable state in this system is whether the hinge is open or closed, so we consider the microstates of the system that correspond to these macrostates. We treat an open hinge as consisting of only a single state, capturing the effect of the many physical microstates in the closing free energy parameters, the hinge closing enthalpy change ΔH_{cl} and the hinge closing entropy change ΔS_{cl}. For a closed hinge, we enumerate the possible binding states more explicitly as shown in Fig. 2. First, any number of the bottom overhangs on the nano-hinge can be involved in base pairing with the ssDNA strands on the AuNP (Fig. 2(A)). For any given base-pairing interaction, any consecutive stretch of adenines on the bottom overhang can bind to any consecutive stretch of equal length of thymines on the ss-

DNA strands on the AuNP (Fig. 2(B)). Each set of consecutive base pairs is associated with a base pairing enthalpy ΔH_{bp} and entropy ΔS_{bp}. In addition, the initial formation of each connection is associated with a binding entropy ΔS_b.

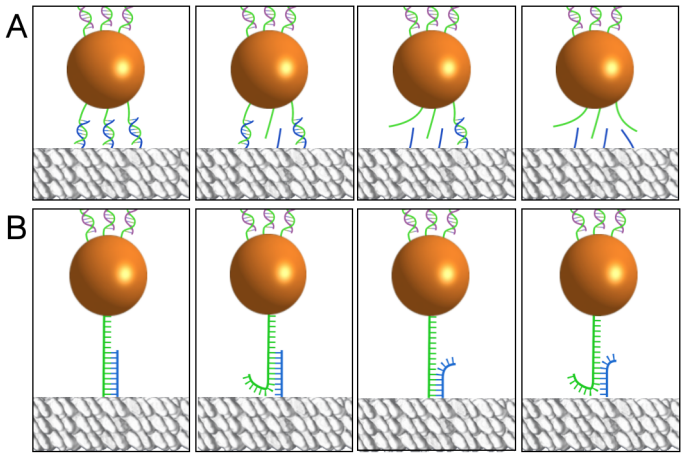

Fig. 2 Schematic illustration of closed nano-hinge states. The AuNP is indicated by the gold sphere, the bottom hinge overhangs by blue lines, top arm overhangs by red lines, and the AuNP strands by green lines. The gray helices represent the bottom arm of the nano-hinge. (A) gives the states on the strand binding level, while (B) gives the states on the base pairing level. In (A) we note that there is one way to bind three connections ("tri-connected", first panel), three ways to bind two connections ("bi-connected", second panel), three ways to bind one connection ("mono-connected", third panel), and one way to bind zero connections ("unconnected", fourth panel). This is described mathematically in Eq. (4). In (B), there are states with no fraying (first panel), states with fraying from the poly-T end (second panel), states with fraying from the poly-A end (third panel), and states with fraying from both ends (fourth panel). This is described mathematically in Eq. (5).

2.3.4 Simplifying assumptions

We do not consider any base-pairing states that involve bulges or internal loops, i.e., unpaired bases internal to a base-paired region, which have a prohibitively high free energy cost. Various experimental results indicate that the free energy cost of such states is at least on the order of 4 kJ/mol. Tanaka *et al.*[41] find that free energies for single A and T bulges at 37 °C are 6.95 ± 4.39 kJ/mol and 4.0 ± 3.9 kJ/mol, respectively. Longer bulges are expected to be similarly costly, as reported by Turner and Matthews in the context of RNA[42]. The cost of interior loops can be approximated using mismatch parameters for an ACA/TTT sequence, which Allawi *et al.* find to be 5.82 ± 0.46 kJ/mol[43]. Similarly, Peyret *et al.* find AA and TT mismatches to have energy costs on the order of 4 kJ/mol[44]. At a cost of at least 4 kJ/mol in addition to the loss of two base stacking interactions, the Boltzmann factor for a state decreases by a factor of $\exp\left[(\Delta G_{\text{bulge}} + 2\Delta G_{bp})/kT\right] \sim 170$ upon the introduction of an interior loop. The introduction of a bulge, however, only results in a reduction of $\exp\left[(\Delta G_{\text{bulge}} + \Delta G_{bp})/kT\right] \sim 30$, since a bulge only removes a single stacking interaction. Consequently, we tested the validity of ignoring bulges by taking bulges into account in an approximate way as follows: We treated bulges of differing lengths as having the same energetic cost, that of a single base bulge reported by Tanaka *et al.*[41], and enumerated all states containing a single bulge of arbitrary size at an arbitrary position within a stack. We find that the impact on the model is minimal: the goodness of fit values are within a few percent, and four of the five fit parameters are within error. The ΔS_b parameter decreases by around 30%, however, to account for the increased entropy provided by the bulged states. Since a quantitatively accurate description of bulges that accounts for differing energetic costs associated with differing bulge lengths increases the computational cost of the model and would have an even smaller effect than our approximation above (since the true energetic cost of a bulge increases with bulge length), we choose to ignore such states.

In addition to neglecting bulges and internal loops, we also do not consider interactions between non-complementary DNA strands or between DNA strands and the origami structure. Experimental hysteresis is averaged out, as discussed in Section 2.2.2. The bulk measurement also averages over differences in individual hinges. In particular, there may be variations in size and DNA surface density of the AuNPs, and the literature demonstrates that DNA origamis do not incorporate strands with perfect efficiency, resulting in variations depending on which strands fail to incorporate[45,46]. Finally, we assume that the enthalpy and entropy of both the nano-hinge and base pairing interactions remain constant over the full range of temperatures that we consider.

2.3.5 Opening probability

In order to compute the probability that the system resides in the states specified above, it is necessary to determine the free energies associated with each state and to compute a partition function. The free energy of each of these microstates is determined by the number of paired bases, the number of connections, and the energy required to close the hinge. Since the temperature is variable, both the enthalpic and entropic parts of the free energies must be considered. Using the open state as a reference free energy $G_{\text{open}} = 0$, we can write

$$\begin{aligned} G_i(T) &= \Delta H_{cl} - T\Delta S_{cl} + N_i(\Delta H_{bp} - T\Delta S_{bp}) + \\ &\quad + 2N_{c,Tot,i}(\Delta H_{\text{term}} - T\Delta S_{\text{term}}) - N_{c,Tot,i}\Delta S_b T. \end{aligned} \tag{1}$$

for each closed microstate i, where T is temperature, $N_{c,Tot,i}$ is the total number of connections (i.e. bottom arm overhangs that have at least a single base paired), N_i is the number of base stacks (since the base pairing energy is associated with the energetic favorability of stacking two consecutive base pairs); ΔH_{cl} and ΔS_{cl} are the hinge closing enthalpy and entropy, respectively; ΔH_{bp} and ΔS_{bp} are the base pairing enthalpy and entropy, respectively; ΔH_{term} and ΔS_{term} are the terminal base pairing enthalpy and entropy, respectively; and ΔS_b is the entropy cost to form duplex DNA from two single strands, which we assume is the same to form the first, second, and third duplexes for multi-valent interactions. The partition function for this system is then

$$Z = 1 + \sum_i \exp\left[-G_i(T)/k_B T\right], \tag{2}$$

where the sum is over all microstates of the system. Since we treat the hinge as consisting of a single open state with free energy $G_{\text{open}} \equiv 0$, the probability that a hinge is in an open state is given by

$$p_{\text{open}} = 1/Z. \tag{3}$$

In order to calculate Z more explicitly, we have to consider the partition function of the closed states, denoted Z_{cs}. Since all closed states are multiplied by a Boltzmann factor corresponding to the free energy cost to close the hinge, denoted by $\Delta G_{cl} = \Delta H_{cl} - T\Delta S_{cl}$, the primary challenge is to account for all possible base pairing states, as illustrated in Fig. 2. To do this for an arbitrary number of overhangs per hinge with potentially differing numbers of bases per overhang, we first denote overhangs of different lengths (i.e. different number of bases) by subscript j, and the number of type j overhangs by $N_{\text{c},j}$. For instance, if we have a hinge with three overhangs, two of which are six bases long (type 1) and one of which is eight bases long (type 2), we would have $N_{\text{c},1} = 2$ and $N_{\text{c},2} = 1$. We then need to account for all possible choices of actually realized connections n_j of type j. The number of possibilities to choose n_j out of $N_{\text{c},j}$ total available connections must also be considered, introducing a binomial coefficient for each j. Combining the above yields

$$Z_{\text{cs}} = \exp\left(-\Delta G_{cl}/k_BT\right)\times \sum_{n_1=0}^{N_{\text{c},1}}\left[\binom{N_{\text{c},1}}{n_1} Z_{\text{S},1}^{n_1} \times \sum_{n_2=0}^{N_{\text{c},2}}\left[\binom{N_{\text{c},2}}{n_2} Z_{\text{S},2}^{n_2} \times \cdots \times \exp\left[(n_1+n_2+\cdots)\Delta S_b T/k_BT\right]\right]\right] \tag{4}$$

where $Z_{\text{S},j}$ is the partition function describing all of the possible base pairing interactions for a single connection of type j. In particular,

$$Z_{\text{S},j} \equiv \sum_{i=1}^{N_{\text{S},j}} (N_T - i + 1)(N_{\text{A},j} - i + 1)\exp\left[-\frac{\Delta G_{\text{term}} + i\Delta G_{bp}}{k_BT}\right] \tag{5}$$

where $N_{\text{S},j}$ is the maximum number of stacks in the type j duplex, N_T is the maximum number of stacks available to the poly-T strand, and $N_{\text{A},j}$ is the maximum number of stacks available to the poly-A strand of type j. Thus, $N_{\text{S},j} = \min\{N_T, N_{\text{A},j}\}$. $\Delta G_{bp} = \Delta H_{bp} - T\Delta S_{bp}$ is the free energy of a single stack, and $\Delta G_{\text{term}} = 2(\Delta H_{\text{term}} - T\Delta S_{\text{term}}) = 2\left[9.6\text{ kJ/mol} - T(0.0172\text{ kJ/(mol K)})\right]$ is the terminal base pairing energy[47]. Note that $N_T - i + 1$ is the number of positions on the poly-T strand at which i consecutive stacks can bind, and that $N_{\text{A},j} - i + 1$ is the number of positions on the poly-A strand at which i consecutive stacks can bind. Thus, their product is the total multiplicity of the state with i bound stacks.

Taking everything together, we therefore have

$$Z = 1 + \exp\left(-\Delta G_{cl}/k_BT\right)\times \sum_{n_1=0}^{N_{\text{c},1}}\left[\binom{N_{\text{c},1}}{n_1} Z_{\text{S},1}^{n_1} \times \sum_{n_2=0}^{N_{\text{c},2}}\left[\binom{N_{\text{c},2}}{n_2} Z_{\text{S},2}^{n_2} \times \cdots \times \exp\left[(n_1+n_2+\cdots)\Delta S_b T/k_BT\right]\right]\right] \tag{6}$$

with $p_{\text{open}} = 1/Z$, where for clarity the ΔG's are not written as functions of temperature, but they retain the temperature dependence indicated in Eq. (1).

Since the fluorescence data is normalized such that the maximum value is 1, we relate the normalized fluorescence to the probability that a hinge is open as follows:

$$F_{\text{norm}} = p_{\text{open}}/p_{\text{max}} \tag{7}$$

where p_{max} is the probability that the hinge is at an angle such that the fluorescence is not quenched in the absence of the NP, i.e., $p_{\text{max}} = \left[1 + \exp\left(-\Delta G_{cl}/k_BT\right)\right]^{-1}$.

2.4 Model fitting

In order to relate the model to the data, we fit the normalized opening probability, $p_{\text{open}}/p_{\text{max}}$, to the experimental normalized fluorescence by varying the four energetic parameters within physically realistic bounds (i.e. $0 \le \Delta H_{cl} \le \infty$ and $-\infty \le \Delta S_{cl}, \Delta H_{bp}, \Delta S_{bp}, \Delta S_b \le 0$). This fit is performed via a non-linear least squares minimization for this bounded set of parameters using a Trust Region Reflective algorithm[48], which is implemented using the Python SciPy package[49].

2.5 Code and data availability

Python code implementing the model is available at `https://github.com/bundschuhlab/PublicationScripts/tree/master/NanoswitchTActuationPrediction`. Data is available upon request.

3 Results & Discussion

In this section, we will first give a short high level overview of our model and then demonstrate how it agrees with the experimental data and expectations based on the literature. Next, we extract mechanistic insights about nano-hinge actuation. Lastly, we demonstrate that the model can be used to guide the design of nano-hinges that can be actuated over a wide range of temperatures.

3.1 A thermodynamic model of thermal nano-hinge actuation

We formulate a thermodynamic model for actuation of the hinge containing an AuNP as shown in Fig. 1(A). Specification of a thermodynamic model requires enumeration of the allowed states of the system, the free energies associated with each state, as well as a relationship between these states and experimental observ-

ables. The macroscopic observable here is the open (fluorescing) or closed (quenched) state of the hinge. We model the system as having a single open state, representing many microstates, which has some unknown free energy cost to transition into the closed state. This free energy cost captures the contribution from all open microstates and consists of an enthalpic component ΔH_{cl} and an entropic component ΔS_{cl}. When the hinge is closed, there are many binding microstates available, but these states are easier to enumerate: when closed, the hinge overhangs are allowed to anneal to the AuNP DNAs, and every combination of consecutive base pairing stacks is allowed. This is shown schematically in Fig. 2. Fig. 2(A) shows the strand-level allowed binding states, and Fig. 2(B) shows the base pair-level allowed binding states. Fraying is allowed from the AuNP strand end, the hinge overhang end, and from both ends. Additionally, the strands are allowed to slide relative to each other without penalty, so that any combination of consecutive bases can anneal (all the way up to the AuNP). Since the hinge overhangs are poly-A and the AuNP overhangs are poly-T, each stack of two consecutive base pairs that forms is associated with the same base pairing free energy with enthalpic component ΔH_{bp} and entropic component ΔS_{bp}. In addition, a terminal free energy with enthalpic component ΔH_{term} and entropic component ΔS_{term} is taken into account for each end of a helix of consecutive base pairs; however, in contrast to the other parameters, this latter contribution is not treated as fit parameters but fixed at literature values[47]. Finally, we impose an entropy cost ΔS_b associated with formation of a duplex. Given these definitions of the states and their free energies, the partition function of the system and thus the probability of a hinge to be in the open state and fluorescing can be calculated as a function of temperature (see section 2.3.5).

3.2 Nano-hinge actuation is quantitatively explained by the thermodynamic model

We fit the temperature dependent opening probability predicted by the thermodynamic model to the experimental normalized fluorescence using a non-linear least squares minimization for the enthalpies and entropies ΔH_{cl}, ΔS_{cl}, ΔH_{bp}, ΔS_{bp}, and ΔS_b (see section 2.4).

A comparison of this fit to the data is shown in Fig. 3, and the best fit parameters are summarized in Table 1. In Fig. 3, a comparison of the fit to the bivalent data is shown in the leftmost panel, while a comparison of the fit to the trivalent data is shown in the middle panel. Note that, although these comparisons are shown separately for clarity, they show the results of a single fit to the bivalent and trivalent data simultaneously. Additionally, each panel shows the average (over each individual actuation curve) root mean squared difference ($\overline{\text{RMS}}$) between the data and model in that panel. In both bivalent and trivalent cases, the model agrees well with the data with a $\overline{\text{RMS}}$ of 0.054 for the bivalent data and of 0.068 for the trivalent data.

We want to emphasize that, while the experimental data is separated by valency rather than overhang length, the experimental actuation curves for the bivalent and trivalent cases differ (as shown in Fig. S1) and thus provide independent tests for the

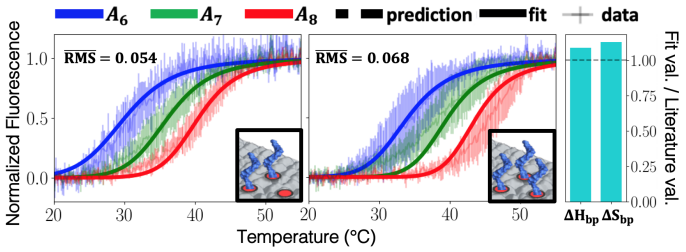

Fig. 3 Model fit to experimental data. The model (bold lines) is fit to bivalent and trivalent data simultaneously, with a bivalent comparison shown in the leftmost panel and a trivalent comparison shown in the middle panel. Each panel contains the averaged root mean squared difference ($\overline{\text{RMS}}$) between the model and the average of the experimental data. In particular $\overline{\text{RMS}}$ is the average over the RMS differences for each curve shown in the panel. The rightmost column shows the ratio between the fit base pairing parameter values and the expected base pairing parameter values from the literature[47].

Table 1 Model described in section 2.3 best fit parameters (used in Fig. 3) in units of kJ/mol for enthalpies and kJ/(mol K) for entropies.

ΔH_{cl}	ΔS_{cl}	ΔH_{bp}	ΔS_{bp}	ΔS_b
0 ± 9	-0.02 ± 0.03	-36.0 ± 1.2	-0.108 ± 0.004	-0.0466 ± 0.0009

model. Thus, the valency based difference is accurately captured by the model without further adjustment of its parameters. We conclude that the thermodynamic model faithfully describes the entire temperature dependence of nano-hinge actuation for six different experimental conditions spanning two different valencies and three different overhang lengths using five fit parameters.

3.3 Optimal base pairing parameters agree with literature values

While we treat the enthalpy ΔH_{bp} and entropy ΔS_{bp} of the base pairing as fit parameters, these have been independently measured by SantaLucia[47] from melting experiments on short DNA oligomers and have been used for decades to quantitatively describe DNA melting. Therefore, it is illustrative to compare our best fit parameters to SantaLucia's values. The rightmost column of Fig. 3 shows that the ratio of our best fit parameters to SantaLucia's values with corrections for salt concentration[50] (details in ESI section S1†, $\Delta H_{bp,SL} = -33.1$ kJ/mol and $\Delta S_{bp,SL} = -0.0955$ kJ/mol K) are close to one. As a further test of the appropriateness of the observed base pairing parameters, we fit the model again while keeping the base pairing enthalpy ΔH_{bp} and entropy ΔS_{bp} at SantaLucia's literature values, corrected for salt conditions[47,50–52] (details in ESI section S1†). These fits are shown in Supplementary Fig. S2, and the fit parameters are given in Table S1. We find an excellent fit if only the base pairing enthalpy is fixed to its literature value and a reasonable fit if base pairing enthalpy and entropy are both fixed at their literature values. These fits are especially reasonable when considering that the effects of divalent salt remain difficult to quantify and mostly affect the entropy[47,51,52].

The good agreement between literature values of the base pairing parameters and the best fit parameters of our model is inter-

esting, since other studies have found that the presence of a DNA origami device can have significant impact on base pairing free energy[15,53]. One possible explanation is that in the experiments underlying these earlier studies the base pairing occurs in a much more geometrically constrained context, which is avoided by the presence of the AuNP coated with longer DNA strands in the experiments that are modeled here. Also, the corrections in these studies are directly to the base pairing free energy[15,53] while we consider enthalphy and entropy separately to model the entire temperature dependence. Since the free energy results from a delicate balance between enthalpic and entropic contributions, the free energy may be more sensitive than enthalpy or entropy alone. We conclude that our fit parameters and literature values for the base pairing parameters agree well, providing further independent validation of our model.

3.4 Optimal closing entropy parameter is consistent with free nano-hinge angle distribution

As is the case with the base pairing parameters, we are able to independently estimate the value of the hinge closing entropy parameter ΔS_{cl}. In order to make this estimation, we calculate the relative entropy between a closed hinge angular probability distribution and a free hinge angular probability distribution (in particular, the angular distribution of a hinge with an incorporated AuNP but no bottom arm hinge overhangs) measured experimentally by Johnson *et al.*[23] (see ESI Fig. S3). The relative entropy between these distributions is given by

$$\Delta S_{\mathrm{rel}} = \sum_i P_{\mathrm{cl},i} \ln\left[\frac{P_{\mathrm{cl},i}}{P_{\mathrm{free},i}}\right] \tag{8}$$

where $P_{\mathrm{cl},i}$ and $P_{\mathrm{free},i}$ are the probabilities that a closed and free hinge have angles within some bin i. This calculation predicts an entropy increase of ≈ 0.02 kJ /(mol K) associated with transition from the closed to the open state. We note, however, that this calculation only takes into account entropy change due to a single degree of freedom (change in nano-hinge angle). There are also out of plane fluctuations of the nano-hinge and fluctuations in the positions and orientation of the AuNP that are restricted by binding. Therefore, this calculation can be interpreted as providing an approximate upper limit of -0.02 kJ/ (mol K) on ΔS_{cl} as well as an order of magnitude estimate for this parameter. This is in good agreement with the fit parameter $\Delta S_{cl} = -0.02 \pm 0.03$, providing yet another independent validation of the model. Furthermore, the value of the best fit parameter near the upper limit suggests that out of plane fluctuations are negligible in this system.

3.5 Averaging over melting and annealing data approximates equilibrium conditions

For our fitting we use the data published by Johnson *et al.*[23] averaged over experimental replicates and direction of temperature change, with the width of the curves corresponding to the standard deviation over all of these data sets (see section 2.2.2 for details). Although we model this system as an equilibrium process, it is important to note that there *is* hysteresis in the experimental data between the annealing, which exhibits a slightly lower transition temperature, and the melting, which exhibits a slightly higher transition temperature. In order to verify that the average of these melting and annealing curves is a good approximation to an equilibrium condition, we perform the thermal actuation experiment at two different rates of temperature change: 2 °C/min (as previously done by Johnson *et al.*[23]) and 0.2 °C/min. For these experiments, we replaced the AuNP with double-stranded DNA linkers to avoid potential AuNP degradation with extended time at elevated temperatures[54]. These experiments reveal that as the rate is decreased, the hysteresis also decreases and both the melting and annealing curves approach the average of the fast rate curves. Additionally, the average of the slow rate curves is similar to the average of the fast rate curves. This data, shown in Fig. S4, illustrates that the averaging is a reasonable approximation to the equilibrium conditions.

Nevertheless, we also test the model in the two extreme assumptions that the true equilibrium is either the melting or annealing data. These fits are shown in Fig. S5, with best fit parameters reported in Table S2. While these fits result in $\overline{\mathrm{RMS}}$ values that are somewhat higher than the fits to averaged data (about 0.07 and 0.08 for bivalent and trivalent, respectively), the values of the base pairing parameters still agree reasonably well with literature values. We conclude that our observations concerning the validity of the thermodynamic model are robust to the details of the treatment of the experimentally observed hysteresis.

3.6 Fraying plays a measurable role in nano-hinge actuation

The thermodynamic model also elucidates the role of sliding and fraying in the binding between hinge overhangs and strands attached to the AuNP. As shown in Fig. 2(B), the model takes into account fraying of the base pairing between hinge and AuNP overhangs at each end as well as arbitrary sliding of the two strands relative to each other (since they are homopolymers). Supplementary Fig. S6 (parameters in Table S3) shows fits for variants of the model in which fraying and sliding (A), fraying (B), and sliding (C) are not allowed (see ESI section S2†). While the $\overline{\mathrm{RMS}}$ values are similar to those in Fig. 3, the agreement with SantaLucia's base pairing parameters is significantly worse for the cases in which fraying is not allowed, suggesting suboptimal annealing states are important in regulating the thermal actuation.

In order to examine this fraying more closely, we calculate the average number of bases paired in a bound connection, given by

$$\langle N_{bp}\rangle = \frac{\sum_{i=1}^{N_{\mathrm{S},j}} (i+1)(N_T - i + 1)(N_{\mathrm{A},j} - i + 1) \exp\left[-\frac{\Delta G_{\mathrm{term}} - \Delta S_b + i\Delta G_{bp}}{k_B T}\right]}{Z_{\mathrm{S},j}}. \tag{9}$$

The results of this calculation (Fig. S7) suggest that the amount of fraying predicted by the model is physically reasonable. In particular, at low temperatures there is a very small amount of fraying, but the fraying increases with temperature.

Interestingly, however, the sliding states do not seem to play as important a role. The $\overline{\mathrm{RMS}}$ values are again similar to those in Fig. 3, but here the base pairing parameters are much closer to expectation than those of the models that exclude fraying. It seems likely, however, that the loss of sliding entropy has sim-

ply been absorbed into the binding entropy, ΔS_b. To see this, we note that the difference between ΔS_b for the model with sliding (see Table 1) and without sliding (see Table S3) is $\Delta\Delta S_b = -0.0466 + 0.0204$ kJ/(mol K) $= -0.0262$ kJ/(mol K). In order to estimate the entropy loss due to the removal of sliding, we can use Boltzmann's equation and the previously enumerated states of the system (see Eq. (5)) in the optimal base pairing state $i = N_{S,j}$. For each connection, the loss of entropy due to the removal of sliding states is given by

$$\Delta S_{\text{slide}} \approx -k_B \ln W = k_B \left[\ln(N_T - N_{S,j} + 1)(N_{A,j} - N_{S,j} + 1)\right], \quad (10)$$

where W is the number of states in the system. For 7 base polyA strands and 23 base polyT strands, $W = 17$ and therefore $\Delta S_{\text{slide}} \approx -0.02$ kJ/(mol K), which is close to $\Delta\Delta S_b$. Furthermore, we would expect that the exact value of ΔS_{slide} to be a little more negative than the estimate given by Eq. (10), since this calculation does not account for suboptimal sliding states. Therefore, the observed $\Delta\Delta S_b = -0.0262$ kJ/(mol K) is consistent with the sliding entropy loss being absorbed into the ΔS_b parameter.

Unfortunately, we do not have a strong *a priori* preference between the ΔS_b values with and without sliding. Thus, the extent to which sliding influences the actuation is unknown, and we conclude that it is prudent to leave sliding states in the model.

3.7 Actuation temperature is driven by the bi-connected states

A limitation of the model is that it is unable to explain experimental observations of "monovalent" hinge data (i.e. data from hinges with only a single overhang). In particular, when Johnson *et al.* constructed monovalent nano-hinges with 6 – 9 base overhangs, they observed no hinge closing for temperatures from 20 °C to 55 °C[23]. This is inconsistent with the model prediction of monovalent A_8 and A_9 actuation at 33.7 °C and 37.5 °C, respectively. This discrepancy could be due to factors well beyond the scope of our model, such as, e.g., slow kinetics of monovalent connections. However, a plausible extension of our model possibly capable of explaining a different behavior for monovalent connections would be to allow the entropy cost of duplex formation ΔS_b to be different for the first, second, and third strands that bind, reflecting the changes in geometry due to the number of strands already bound. Accordingly, in this section we discuss an alternative model in which we allow the parameter ΔS_b to vary depending on how many other strands are already bound. This then becomes three parameters, $\Delta S_{b,1}$, $\Delta S_{b,2}$, and $\Delta S_{b,3}$, which correspond to the entropy costs to bind the first strand, the second strand, and the third strand, respectively. We will refer to this model as the "variable ΔS_b" or "*varS*" model. Similarly, the previous model will be referred to as the "constant ΔS_b" or "*conS*" model.

The introduction of the additional parameters results in several degeneracies that complicate the analysis somewhat. To counteract these degeneracies, we first fix ΔS_{cl} to its best fit value in *conS* model, since it is nearly degenerate with $\Delta S_{b,1}$ (they are only differentiated by the unconnected ($N_c = 0$) closed state). This value is also consistent with our independent estimation of the hinge closing entropy of $\Delta S_{\text{cl}} \approx -0.2$ kJ/(mol K) using the angular probability distributions of the nano-hinge in each state (see section 3.4). Even with ΔS_{cl} fixed, we still find that there is not one optimal set of parameters but rather a whole volume in the $\Delta S_{b,1}$-$\Delta S_{b,2}$-$\Delta S_{b,3}$ space that results in nearly indistinguishably good fits. Thus, in order to analyze the *varS* model, we systematically vary all three ΔS_b parameters and measure the best fit parameters and goodness of fit values. To summarize the results of this analysis, we determine the volume in three dimensional $\Delta S_{b,1}$-$\Delta S_{b,2}$-$\Delta S_{b,3}$ space for which the average RMS value over all six curves is below 0.058 (and thus within 0.002 of the minimum since we do not find any regions with an average RMS value below 0.056). This volume is shown in Fig. 4(A), and ESI Fig. S8 shows the fit for a representative point $(\Delta S_{b,1}, \Delta S_{b,2}, \Delta S_{b,3}) = (-0.05, -0.01, -0.05)$ kJ/(mol K) inside of it. This demonstrates that that the degenerate near-optimal volume is bounded by (roughly) $\Delta S_{b,3} < -0.05$ kJ/(mol K), $\Delta S_{b,2} > -0.03$ kJ/(mol K), and $\Delta S_{b,1} > -0.08$ kJ/(mol K) $- \Delta S_{b,2}$. Note that the point with $\Delta S_{b,1} = \Delta S_{b,2} = \Delta S_{b,3} = -0.04$ kJ/(mol K) obtained for the *conS* model falls *outside* of this range consistent with its slightly elevated average RMS of 0.061. Additionally, this near-optimal volume is also colored in Fig. 4(A) according to the actuation temperature of the monovalent A_9 hinge, demonstrating that values of $\Delta S_{b,2}$ that are closer to zero result in lower monovalent A_9 actuation temperatures mostly consistent with experimental observation.

Next, we investigate the ratio of the best fit base pairing parameters ΔH_{bp} and ΔS_{bp} to their respective expected values from the literature (i.e. the ratios shown in the rightmost panel of Fig. 3) in the *varS* model. Fig. 4(B) shows these as a function of $\Delta S_{b,2}$ (where we optimize over the other parameters for each $\Delta S_{b,2}$) and demonstrates that the base pairing parameters increasingly deviate from expectation as $\Delta S_{b,2}$ becomes more negative. For reference, the values of $\Delta S_{b,2}$ corresponding to the near-optimal volume in Fig. 4(A) are shaded in green, and the *conS* ΔS_b value is marked by a vertical red line. The better agreement of the base pairing parameters with expectation in the $\Delta S_{b,2}$ range preferred by the *varS* model over its value in the *conS* model provides further evidence of the superiority of the *varS* model. This dependence of the base pairing parameters on $\Delta S_{b,2}$ also points toward values of $\Delta S_{b,2}$ close to zero to be preferable in agreement with where we have found the monovalent actuation temperature to be the lowest.

Finally, we consider the physics of the system in order to understand the origin of the near-optimal region of *varS* parameters. In particular, we note that values of $\Delta S_{b,2}$ close to zero and values of $\Delta S_{b,3}$ that are strongly negative (as is the case in the near-optimal parameter volume) have a similar qualitative effect. In particular, both of these requirements tend to favor states with two overhangs bound (bi-connected) compared to states with three overhangs bound (tri-connected). This suggests that conditions in which bi-connected states dominate over tri-connected ones (in the trivalent case) provide a better fit. In order to verify these observations, we next plot the fraction of closed states that are bi-connected at the actuation temperature. In order to visualize this data, we note that the upper limit on the tri-connected fraction

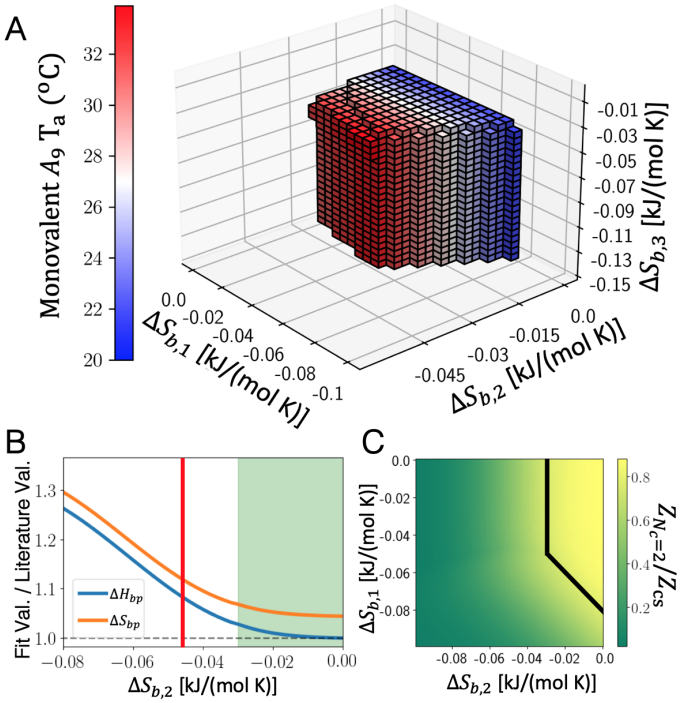

Fig. 4 *VarS* model analysis. (A) Near-optimal volume for which average *varS* RMS over all six actuation curves used for fitting (6, 7, and 8 base overhangs for both bivalent and trivalent hinges) is between 0.056 and 0.058. This volume is bounded by (roughly) $\Delta S_{b,3} < -0.05$ kJ/(mol K), $\Delta S_{b,2} > -0.03$ kJ/(mol K), and $\Delta S_{b,1} > -0.08$ kJ/(mol K) $- \Delta S_{b,2}$. ΔS_{cl} was fixed at its *conS* value and an optimization was performed over the remaining parameters for each value of ($\Delta S_{b,1}$, $\Delta S_{b,2}$, $\Delta S_{b,3}$). Colors indicate predicted monovalent 9 base actuation temperature. (B) Ratio of base pairing fit parameters to their SantaLucia values[47] shown as a function of $\Delta S_{b,2}$. ΔS_{cl} was fixed at its optimal *conS* value, and an optimization was performed over the remaining parameters. The shaded green region indicates the near-optimal values of $\Delta S_{b,2}$ (corresponding to the volume in (A)), and the red line indicates the value of the *conS* optimal ΔS_b. (C) Fraction of *varS* closed states that are bi-connected at the actuation temperature averaged over trivalent 6, 7, and 8 base nano-hinges. The scan is performed over $\Delta S_{b,1}$-$\Delta S_{b,2}$ space with $\Delta S_{b,3}$ set to its upper bound of -0.05 kJ / (mol K) and ΔS_{cl} fixed at its *conS* value, and other parameters are optimized. The area in the upper right enclosed by the black lines corresponds to the near-optimal volume in panel (A).

occurs at the upper (least negative) bound on $\Delta S_{b,3}$, and therefore show the bi-connected closed fraction over the slice of the near-optimal volume corresponding to $\Delta S_{b,3} = -0.05$ kJ / (mol K). This data is shown in Fig. 4(C), with the near-optimal region bounded in black lines. The bi-connected fraction is large in the near-optimal region and small in the rest of the parameter space, confirming the hypothesis that near-optimal *varS* parameter values correspond to large fractions of bi-connected closed states at the actuation temperature, a key insight of this analysis.

It is important to note that, although this suggests that bi-connected states dominate during the transition (and thus set the actuation temperature), this does not preclude a significant fraction of tri-connected states occurring at low temperatures. Indeed, in ESI Fig. S9, we demonstrate that for the parameters used in ESI Fig. S8, tri-connected states are more prevalent than bi-connected states at low temperatures for a trivalent nano-hinge. As the temperature increases towards the actuation temperature, however, the lower entropy of these states causes these states to become unfavorable compared to the higher entropy bi-connected states. This represents an important and counter-intuitive insight into this actuation process: Although one might naïvely expect that the most favorable low temperature state to be the one that, to first order, controls the actuation behavior, we have shown that, due to entropic effects, this is not the case.

Interestingly, despite the dominance of the bi-connected states at the transition in the trivalent case, the experimental data clearly differs between the bivalent and the trivalent case, and the model quantitatively captures this difference (see ESI Fig. S1). Since the tri-connected states are not important at the transition, this difference between the bivalent and the trivalent case must come primarily from configurational entropy: in the bivalent case there is only one bi-connected state, whereas in the trivalent case there are three such states. Therefore, we conclude that the additional configurational entropy in the trivalent case is the primary driver of the shifts of the actuation points toward higher temperatures.

Overall, the analysis of the *varS* model has shown that reasonable choices of individual strand binding entropies can produce the relatively low monovalent A_9 actuation temperatures expected from experimental data. Additionally, the analysis contained in this section provides a deeper understanding of the physics of this system which likely has consequences for any system in which temperature-mediated strand dissociation drives actuation. In particular, the insight that the most tightly bound state may not drive the transition behavior should be generally applicable.

3.8 Quantitative model allows design of devices with arbitrary transition temperatures

Both the *conS* and *varS* models show excellent agreement with experimental bivalent and trivalent data, and they are able to quantify the change in actuation response due to a change in overhang valency and length. If this feature is predictive, it could be useful to design actuation at a desired temperature without costly experimental trial and error. The models predict that manipulation of overhang design parameters can be used to achieve actuation at essentially any desired temperature in the range from about 30 °C to 45 °C as shown in Fig. 5(A). Importantly, while the actuation temperatures in Fig. 5(A) are calculated using the *conS* model (with the best fit parameters from Table 1) these predictions differ by at most 1.2 °C when instead performing them with the *varS* model for several diverse choices of the entropies $\Delta S_{b,1}$, $\Delta S_{b,2}$, and $\Delta S_{b,3}$ in the near-optimal volume (ESI Fig. S10).

In order to validate the ability of these predictions to guide design, we show in Fig. 5(B) that three of these predicted actuation curves agree very well ($\overline{\text{RMS}} = 0.066$) with experimental data that was not used in model development. This data corresponds to AuNP nano-hinges with: two 9-base poly-A overhangs ($A_{9,9}$), previously published by Johnson *et al.*[23]; two 6-base overhangs and one 8-base overhang ($A_{6,6,8}$); and two 8-base overhangs and

one 6-base overhang ($A_{6,8,8}$). The two latter data sets are original to this work and thus their raw melting and annealing curves are shown in Fig. S11. We conclude that the model can be used to design overhang combinations with essentially arbitrary actuation temperatures in the range from about 30 °C to 45 °C.

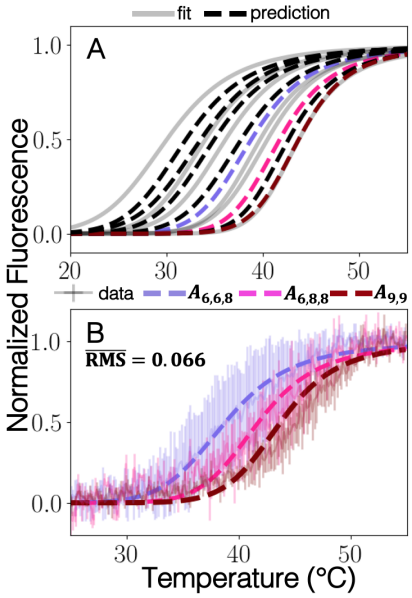

Fig. 5 (A) Temperature spread of predicted actuation curves for hypothetical nano-hinges with variable overhang length and valency using the the best fit parameters of the *conS* model (given in Table S4). Solid and grayed lines are the curves fit to data (trivalent and bivalent 6, 7, and 8 base overhangs), while dashed lines indicate predictions. The violet, pink, and maroon dashed lines indicate predictions validated (in the same colors) in (B). A complete description of the predicted designs sorted by actuation temperature can be found in Table 2. The actuation temperature is defined such that $p_{\text{open}}(T_a) = 0.5$. As mentioned above, (B) gives validation of the $A_{6,6,8}$, $A_{6,8,8}$, and $A_{9,9}$ predictions via a comparison to experimental data (plotted with non-bolded lines in the same colors) which were not used to create or fit the model.

Table 2 Actuation temperatures, defined such that $p_{\text{open}}(T_a) = 0.5$, of predictions shown in bold, dashed lines in Fig. 5. The designs are ordered by increasing actuation temperature, and therefore can be matched to the corresponding curve in Fig. 5. Each number in the hinge design column corresponds to the length of an overhang, so designs with two numbers are bivalent hinges and designs with three numbers are trivalent hinges. Actuation temperatures can be tuned to within 3 °C of any desired temperature between 30 °C and 45 °C

Design	T_a (°C)	Design	T_{act} (°C)
5,6,6	32.0	6,6,8	38.8
6,7	33.6	6,8,8	41.8
5,6,7	35.0	7,8,8	42.7
5,6,8	37.8	9,9	43.7

We also considered the possibility of extrapolation of the model to higher and lower temperatures. Johnson *et al.*, however, did not observe transitions in the case of a trivalent hinge with 9-base overhangs ($A_{9,9,9}$) up to 55 °C[23]. This disagrees with the model prediction of an equilibrium actuation temperature of 46.8 °C for $A_{9,9,9}$ (and similar values in the *varS* case), so it would seem that the model should not be extrapolated to temperatures above the previously indicated 45 °C. Since the nano-hinges themselves melt around 60 °C[23,55,56], it is not entirely unexpected that the model begins to break down at higher temperatures. As the temperature increases and individual sections of the hinge begin to melt, the hinge may become more flexible, effectively decreasing ΔG_{cl} and thus increasing the probability of closed states.

At lower temperatures, Johnson *et al.* did not observe actuation in either a bivalent or trivalent hinge with 5-base overhangs ($A_{5,5}$ and $A_{5,5,5}$) down to 20 °C[23]. This represents a discrepancy of only a few degrees with the model prediction of equilibrium actuation temperatures of 20.9 °C and 25.5 °C for $A_{5,5}$ and $A_{5,5,5}$, respectively (and similar values in the *varS* case). This suggests there may be effects that are not captured by the model below 30 °C.

4 Conclusions

The fast, accurate, and predictive thermodynamic DNA origami actuation model developed in this work offers a viable alternative to computationally costly molecular dynamics modeling in the design of dynamic DNA origami devices. We have shown that not only is it useful as a design tool, but it is able to provide mechanistic insight into the actuation process, in particular by revealing the importance of entropic considerations to thermal transitions. Additionally, the creation of increasingly complex dynamic DNA devices necessitates increasingly computationally efficient modelling[2], of which statistical mechanics is likely to be an important part. This type of model is in principle applicable to any device that is actuated by melting/annealing of DNA duplexes, and similar methods have been shown to be applicable to other dynamic structures[15]. Attempts to use statistical mechanics methods to model a wider range of devices is an important area of future research. Furthermore, incorporation of kinetics using transition matrices acting on microstates (such as the ones defined here) to capture non-equilibrium effects, as well as the integration of statistical mechanics models with molecular simulations to elucidate fine-grained detail, would represent important contributions to the field.

Conflicts of interest

There are no conflicts of interest to declare.

Acknowledgements

We thank the Winter lab for providing nanoparticles for the additional experiments and valuable feedback on the work. This material is based upon work supported by the National Science Foundation under Grant No. DMR-1719316 to RB and by the Department of Energy under Grant no. DE-SC0017270 to CC.

References

1 P. W. Rothemund, *Nature*, 2006, **440**, 297–302.
2 M. DeLuca, Z. Shi, C. E. Castro and G. Arya, *Nanoscale Horiz.*, 2020, **5**, 182–201.
3 A. E. Marras, L. Zhou, H.-J. Su and C. E. Castro, *PNAS*, 2015, **112**, 713–718.
4 S. M. Douglas, I. Bachelet and G. M. Church, *Science*, 2012, **335**, 831–834.

5 H. Ijäs, I. Hakaste, B. Shen, M. A. Kostiainen and V. Linko, *ACS Nano*, 2019, **13**, 5959–5967.

6 P. Ketterer, E. M. Willner and H. Dietz, *Sci. Adv.*, 2016, **2**, e1501209.

7 D. Zhao, J. V. Le, M. A. Darcy, K. Crocker, M. G. Poirier, C. Castro and R. Bundschuh, *Biophys. J.*, 2019, **117**, 2204–2216.

8 J. V. Le, Y. Luo, M. A. Darcy, C. R. Lucas, M. F. Goodwin, M. G. Poirier and C. E. Castro, *ACS Nano*, 2016, **10**, 7073–7084.

9 T. Gerling, K. F. Wagenbauer, A. M. Neuner and H. Dietz, *Science*, 2015, **347**, 1446–1452.

10 E. Kopperger, J. List, S. Madhira, F. Rothfischer, D. C. Lamb and F. C. Simmel, *Science*, 2018, **359**, 296–301.

11 S. Nummelin, B. Shen, P. Piskunen, Q. Liu, M. A. Kostiainen and V. Linko, *ACS Synth. Biol.*, 2020, **9**, 1923–1940.

12 F. C. Simmel, B. Yurke and H. R. Singh, *Chem. Rev.*, 2019, **119**, 6326–6369.

13 D. Y. Zhang and G. Seelig, *Nat. Chem.*, 2011, **3**, 103–113.

14 B. Yurke, A. J. Turberfield, A. P. Mills, F. C. Simmel and J. L. Neumann, *Nature*, 2000, **406**, 605–608.

15 A. E. Marras, Z. Shi, M. G. Lindell III, R. A. Patton, C.-M. Huang, L. Zhou, H.-J. Su, G. Arya and C. E. Castro, *ACS Nano*, 2018, **12**, 9484–9494.

16 C. Mao, W. Sun, Z. Shen and N. C. Seeman, *Nature*, 1999, **397**, 144–146.

17 J. M. Majikes, L. C. Ferraz and T. H. LaBean, *Bioconjugate Chem.*, 2017, **28**, 1821–1825.

18 D. Liu, A. Bruckbauer, C. Abell, S. Balasubramanian, D.-J. Kang, D. Klenerman and D. Zhou, *J. Am. Chem. Soc.*, 2006, **128**, 2067–2071.

19 T. Li and M. Famulok, *J. Am. Chem. Soc.*, 2013, **135**, 1593–1599.

20 S. Modi, M. Swetha, D. Goswami, G. D. Gupta, S. Mayor and Y. Krishnan, *Nat. Nanotechnol.*, 2009, **4**, 325–330.

21 P. M. Arnott and S. Howorka, *ACS Nano*, 2019, **13**, 3334–3340.

22 V. A. Turek, R. Chikkaraddy, S. Cormier, B. Stockham, T. Ding, U. F. Keyser and J. J. Baumberg, *Adv. Funct. Mater.*, 2018, **28**, 1706410.

23 J. A. Johnson, A. Dehankar, J. O. Winter and C. E. Castro, *Nano Lett.*, 2019, **19**, 8469–8475.

24 N. Liu and T. Liedl, *Chem. Rev.*, 2018, **118**, 3032–3053.

25 T. Bayrak, N. S. Jagtap and A. Erbe, *Int. J. Mol. Sci.*, 2018, **19**, 3019.

26 A. O. Govorov and H. H. Richardson, *Nano today*, 2007, **2**, 30–38.

27 C.-Y. Li, E. A. Hemmig, J. Kong, J. Yoo, S. Hernández-Ainsa, U. F. Keyser and A. Aksimentiev, *ACS Nano*, 2015, **9**, 1420–1433.

28 N. Wu, D. M. Czajkowsky, J. Zhang, J. Qu, M. Ye, D. Zeng, X. Zhou, J. Hu, Z. Shao, B. Li *et al.*, *J. Am. Chem. Soc.*, 2013, **135**, 12172–12175.

29 J. Yoo and A. Aksimentiev, *PNAS*, 2013, **110**, 20099–20104.

30 T. E. Ouldridge, A. A. Louis and J. P. Doye, *J. Chem. Phys.*, 2011, **134**, 02B627.

31 P. Šulc, F. Romano, T. E. Ouldridge, L. Rovigatti, J. P. Doye and A. A. Louis, *J. Chem. Phys.*, 2012, **137**, 135101.

32 B. E. Snodin, F. Randisi, M. Mosayebi, P. Šulc, J. S. Schreck, F. Romano, T. E. Ouldridge, R. Tsukanov, E. Nir, A. A. Louis *et al.*, *J. Chem. Phys.*, 2015, **142**, 06B613_1.

33 R. Sharma, J. S. Schreck, F. Romano, A. A. Louis and J. P. Doye, *ACS Nano*, 2017, **11**, 12426–12435.

34 C. Maffeo and A. Aksimentiev, *Nucleic Acids Res.*, 2020, **48**, 5135–5146.

35 D.-N. Kim, F. Kilchherr, H. Dietz and M. Bathe, *Nucleic Acids Res.*, 2012, **40**, 2862–2868.

36 K. Pan, W. P. Bricker, S. Ratanalert and M. Bathe, *Nucleic Acids Res.*, 2017, **45**, 6284–6298.

37 J. Y. Lee, J. G. Lee, G. Yun, C. Lee, Y.-J. Kim, K. S. Kim, T. H. Kim and D.-N. Kim, *ACS nano*, 2021, **15**, 1002–1015.

38 N. Srinivas, T. E. Ouldridge, P. Šulc, J. M. Schaeffer, B. Yurke, A. A. Louis, J. P. Doye and E. Winfree, *Nucleic Acids Res.*, 2013, **41**, 10641–10658.

39 P. Irmisch, T. E. Ouldridge and R. Seidel, *J. Am. Chem. Soc.*, 2020, **142**, 11451–11463.

40 E. Stahl, T. G. Martin, F. Praetorius and H. Dietz, *Angew. Chem.*, 2014, **126**, 12949–12954.

41 F. Tanaka, A. Kameda, M. Yamamoto and A. Ohuchi, *Biochemistry*, 2004, **43**, 7143–7150.

42 D. H. Turner and D. H. Mathews, *Nucleic Acids Res.*, 2010, **38**, D280–D282.

43 H. T. Allawi and J. SantaLucia Jr, *Nucleic Acids Res.*, 1998, **26**, 2694–2701.

44 N. Peyret, P. A. Seneviratne, H. T. Allawi and J. SantaLucia, *Biochemistry*, 1999, **38**, 3468–3477.

45 M. T. Strauss, F. Schueder, D. Haas, P. C. Nickels and R. Jungmann, *Nature communications*, 2018, **9**, 1–7.

46 K. F. Wagenbauer, C. H. Wachauf and H. Dietz, *Nature communications*, 2014, **5**, 1–7.

47 J. SantaLucia, *PNAS*, 1998, **95**, 1460–1465.

48 M. A. Branch, T. F. Coleman and Y. Li, *SIAM Journal on Scientific Computing*, 1999, **21**, 1–23.

49 P. Virtanen, R. Gommers, T. E. Oliphant, M. Haberland, T. Reddy, D. Cournapeau, E. Burovski, P. Peterson, W. Weckesser, J. Bright, S. J. van der Walt, M. Brett, J. Wilson, K. Jarrod Millman, N. Mayorov, A. R. J. Nelson, E. Jones, R. Kern, E. Larson, C. Carey, İ. Polat, Y. Feng, E. W. Moore, J. Vand erPlas, D. Laxalde, J. Perktold, R. Cimrman, I. Henriksen, E. A. Quintero, C. R. Harris, A. M. Archibald, A. H. Ribeiro, F. Pedregosa, P. van Mulbregt and SciPy 1.0 Contributors, *Nat. Methods*, 2020, **17**, 261–272.

50 R. Owczarzy, B. G. Moreira, Y. You, M. A. Behlke and J. A. Walder, *Biochemistry*, 2008, **47**, 5336–5353.

51 M. T. Record and T. M. Lohman, *Biopolymers: Original Research on Biomolecules*, 1978, **17**, 159–166.

52 D. Erie, N. Sinha, W. Olson, R. Jones and K. Breslauer, *Biochemistry*, 1987, **26**, 7150–7159.

53 Z. Shi and G. Arya, *Nucleic Acids Res.*, 2020, **48**, 548–560.

54 F. Li, H. Zhang, B. Dever, X.-F. Li and X. C. Le, *Bioconjugate Chem.*, 2013, **24**, 1790–1797.

55 X. Wei, J. Nangreave, S. Jiang, H. Yan and Y. Liu, *J. Am. Chem. Soc.*, 2013, **135**, 6165–6176.

56 C. E. Castro, F. Kilchherr, D.-N. Kim, E. L. Shiao, T. Wauer, P. Wortmann, M. Bathe and H. Dietz, *Nat. Methods*, 2011, **8**, 221.